ACFA Joint Linear Collider Physics and Detector Working Group Study Report
Draft

ACFA Joint Linear Collider
Physics and Detector Working Group

March 30, 2001

Contents

Chapter 12

Calorimetry

12.1 Design Criteria

One of the most important physics to study at LC is precision study of Higgs boson produced in a reaction $e^+e^- \to Z^0H$. Large backgrounds to this process from W^+W^- and Z^0Z^0 pair production should be removed by b-tagging and reconstructed 2-jet masses. Precision study of weak couplings and top properties also need precise event reconstruction using 2-jet masses under up to 8-jet environment. We therefore set a design criteria for the calorimeter system in combination with the central tracker such that the 2-jet mass resolution be as good as the natural width of weak bosons for excellent W/Z identification. Based on this criteria, the baseline detector model has been made and simulation studies has been carried out.

In order to achieve the required 2-jet mass resolution, we set target energy resolution for calorimeters to be

$$\frac{\sigma_E}{E} = \frac{15\%}{\sqrt{E(\mathrm{GeV})}} \oplus 1\% \quad \text{for e}/\gamma\text{, and}$$
$$\frac{\sigma_E}{E} = \frac{40\%}{\sqrt{E(\mathrm{GeV})}} \oplus 2\% \quad \text{for hadrons,}$$

with reasonably fine granularity. In addition, the calorimter should have position resolution better than 1 mm to achieve precise track-cluster association for jet reconstruction.

Fig. 12.1 shows an example of 2-jet mass resolution obtained by quick simulation with the baseline detector for reaction $e^+e^- \to W^+W^-$ at $\sqrt{S}$ = 400 GeV. Obtained mass resolution of 2.9 GeV with

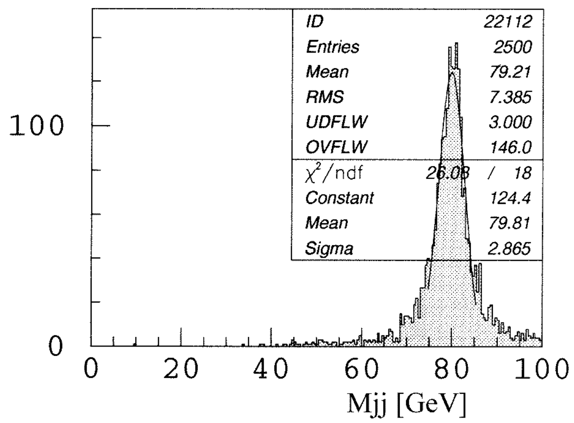

Figure 12.1: An example of 2-jet mass resolution with kinematical fit obtained by quick simulation with the baseline detector for reaction $e^+e^- \to W^+W^-$ at $\sqrt{S} = 400$ GeV.

kinematical fit is reasonably good taking into account that anlysis algorithm and paramteters are not yet optimized very well. Various origins of the width are decomposed in the table 12.1. Each contribution was calculated by replacing each information with generator information.

Natural width of W	$\sim$ 1.6 GeV (in terms of σ)
Neutrino escape	$\sim$ 0.8 GeV
CDC momentum resolution	$\sim$ 1.3 GeV
CAL energy resolution	$\sim$ 1.2 GeV
Cluster-track association	$\sim$ 1.9 GeV
Jet clustering	$\sim$ 1.1 GeV
Total Width	$\sim$ 3.3 GeV (without kinematical fit)

Table 12.1: Various contributions to the width of 2-jet mass for reaction $e^+e^- \to W^+W^-$ at $\sqrt{S} = 400$ GeV.

It has been widely known that in order to achieve the best event reconstruction, tracking information should be used for charged particles, while calorimeter information should be used only for neutral particles. For this purpose, calorimeter hits generated by charged particles should be precisely identified and deleted. Therefore, excellent clustering followed by precise track-cluster association plays essentail role in analysis. This conventional method has been used for analysis of quick-simulation data. However, existence of neutral objects are identified solely by energy-momentum unbalance of associated cluster and track, which does not not require very fine granularity.

From the table, it is seen that more improvements in track-cluster associaction algorithm and in hadron clustering should further improve this result. Needless to say, however, verification with full simulation is indispensible to validate/optimize the baseline parameters.

12.2 Baseline Design

The JLC calorimeter system is characterized by :

- excellent hadron energy resolution;
- reasonably fine granularity;
- whole calorimter system inside of the superconducting solenoid.

Required hadron energy resolution of $40\%/\sqrt{E}$ can only be achieved with compensation, which means that calorimeter signals for EM particles and for hadrons have the same amplitude. There are two ways to acheive the compensation; either hardware compensation or software compensation. Software compensation, first adopted by H1 liq.Ar calorimter [1], requires very fine granularity to apply to LC detectors aimed at precision physics, and thus results in very high cost. We therefore chose hardware-compensation with tile/fiber technique as the a baseline design. By adopting hardware compensation, we can de-couple energy resolution and granularity ; the best energy resolution can be achieved regardless the granularity, and granularity can be determined only by the criteria from topological reconstruction. The tile/fiber calorimeter has following features:

- Essentially crackless hermeticity;
- Capability for very fine longitudinal segmentation;
- Easy to design projective tower layout;
- Easy to integrate preshower and shower-max detectors;
- Reasonable transverse segmentation;

- Less expensive than crystals and liq.Ar.

In addition, the hardware compensation results in following features:

- Excellent hadron energy resolution and linearity;
- High density;
- Reasonable EM energy resolution;
- Relatively low light yield.

Our analysis based on quick simulations indicates that very fine granularity is not necessary for calorimeter. Therefore present baseline design is considered to be almost optimum for the hadron calorimeter (HCAL). For the EM calorimeter (EMC), on the other hand, very fine granularity might be required for precise event topology reconstruction, even though quick simulation tells us that present granularity shows high performance. In that case software compensation would be another option. Further simulation analysis will answer this question. We also need excellent preshower detector (PSD) and shower-max detector (SMD) for $e/\gamma/\pi^{\pm}/\pi^{0}$ separation, two-cluster identification, and track-cluster association. To have plural layers of shower position detector (SPD) in EMC enables precise measurement of off-vertex photon direction.

All the calorimter system, including the photon detectors, are designed to be located inside of the 3 Tesla magnetic field. We therefore need high-gain high-sensitivity photon detectors operational in the strong magnetic field, since hardware compensation results in relatively poor photon yiled compared to the usual sampling calorimeters. We discuss such photon detectors in a separate section.

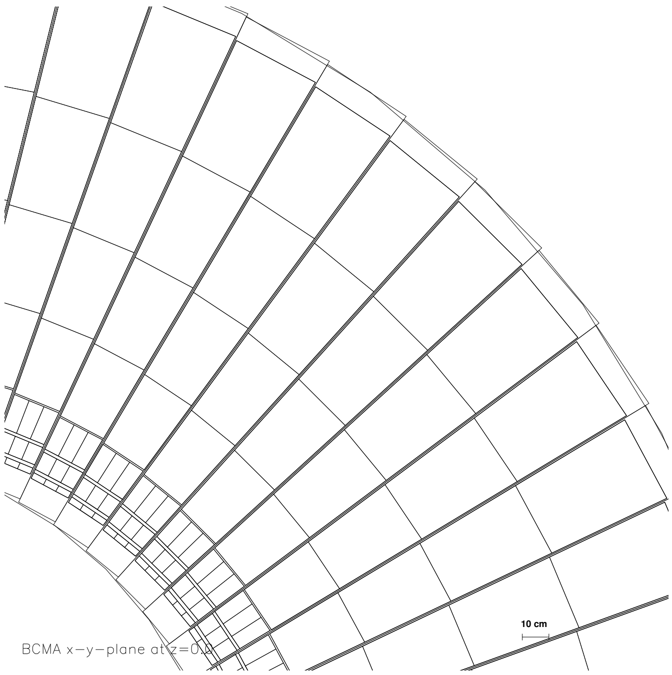

Figure 12.2: Configuration of the baseline design of barrel calorimeter system (x-y cross section) implemented into a full simulator.

The GEANT3 drawing of the baseline-design barrel calorimeter is shown in Fig. 12.2. Inner and outer radii of the barrel calorimeter are 160 cm and 340 cm, respectively, and the length is ±180 cm. Inner radius of the endcap calorimeter is 50 cm, and the front face locates at $z = \pm 190$ cm. Angular coverage of the endcap calorimeter with full-thickness therefore extends to $|\cos\theta| < 0.966$, while partial-thickness coverage extends to $|\cos\theta| < 0.991$. The calorimeter is an array of super-towers with pointing geometry

		2T-case	3T-case	
Barrel Inner Radius		250cm	160cm	
Barrel Outer Radius		400cm	340cm	
Endcap Inner Radius		50cm	50cm	
Endcap Face Z-location		290cm	190cm	
Angular Coverage				
Full Thickness		|cosθ|<0.985	|cosθ|<0.966	
Partial Thickness		|cosθ|<0.994	|cosθ|<0.991	
SHmax Detector		Sintillator Strip (1cm-wide)	Sintillator Strip (1cm-wide)	option= Si-pad (1cm x 1cm)
Thickness				
PreSH		4Xo	4Xo	4mm-Pb x 6 layers
EMC		23Xo	23Xo	4mm-Pb x 32 layers
HCAL		6.5λo	6.5λo	8mm-Pb x 130 layers
Granurality				
PS/EMC	transverse	6cm x 6cm (24mrad)	4cm x 4cm (24mrad)	
	longitudinal	3 sections	3 sections	6+12+20 layers
HCAL	transverse	18cm x 18cm (72mrad)	12cm x 12cm (72mrad)	
	longitudinal	4 sections	4 sections	25+30+35+40 layers

Table 12.2: Parameters of the calorimeter system implemented into a full simulator. 2 Tesla option is the previous large detector option, and 3 Tesla option is a new detector design.

with small offset. One super-tower is composed, from the inner-radius to the outer-radius, of PSD (3×3 in a super-tower), SMD, EMC-1(3×3), SPD, EMC-2(3×3), HCAL-1, HCAL-2, HCAL-3, and HCAL-4. Parameters of these sub-detectors are summarized in Table 12.2. There are about 2000 super-towers in the barrel calorimeter, and about 3000 in total in the endcap calorimeters. One super-tower has readout channels of 31 and 48 for calorimetric measurement and for position measurement, respectively.

There are 2 Tesla option and 3 Tesla option, and detector sizes are smaller for the latter. All the parameters in the table are the first trials, and need optimization with full simulation.

12.2.1 EM Calorimter (EMC)

EMC is a sampling calorimeter composed of 4mm-thick lead plates and 1mm-thick plastic scinitllator plates. Photons from the scintillator plates (tiles) are read out via wavelength shifting fibers (WLS fibers) embedded in the tiles, and then transfered through clear fibers to photon detectors (tile/fiber technique). Additional 1mm-thick acryl plates are stacked on the tile assembly to accomodate clear fibers. This sampling frequency is expected to achieve stochastic term of the EM energy resolution of $15\%/\sqrt{E}$, provided that photon statistics does not contribute.

EMC is longitudinally divided into PSD, EMC1 and EMC2, to improve hadron/electron identification. Thicknesses of these sections are 4.3 X_0 (radiation length), 8.6 X_0, and 14.3 X_0, respectively. We expect pion rejection better than 1/1000 with electron efficiency of 98% when used with HCAL information. Transverse cell size of EMC is 4cm×4cm in the baseline design, and 3×3 EMC cells cover one HCAL cell. This transverse size is limited by technical feasibility of small tiles and cost.

12.2.2 Hadron Calorimter (HCAL)

HCAL is composed of 8mm-thick lead plates, 2mm-thick plastic scinitllator plates, and 1mm-thick fiber-routing acryl plates. HCAL also has tile/fiber configuration. This sampling frequency was expected to achieve stochastic term of the hadron energy resolution of $40\%/\sqrt{E}$, provided that photon statistics did not contribute.

HCAL is longitudinally divided into four sections with thicknesses of 1.25 λ_0 (interaction length), 1.5 λ_0, 1.75 λ_0, and 2.0 λ_0. Total thickness including EMC is 7.5 λ_0. Transverse segment size of HCAL is 12 cm, which covers 72 mrad at $\theta = 90°$ seen from the interaction point.

Number of longitudinal segmentation is limited only by number of photon-detector channels. Improvement in multi-channel photon detecotrs enables much finer longitudinal segmentation, and thus enables more sophisticated clustering and two-cluster separation algorithms. Transverse segment size, on the other hand, is limited by cost, and it seems difficult to make it much smaller.

12.2.3 Shower-Max Detector(SMD) and Shower-Position Detector(SPD)

The purpose of SMD is π^0/γ identification, precise measrement of cluster position for track-cluster association, and two-cluster recognition. SMD also improves $e/\pi^{\pm}$ separation by transverse signal distribution. For this purpose, fine segmentation is necessary for SMD. Also needed is wide dynamic range to detect minimum-ionizing particles (MIP) and developing EM showers simultaneously.

The baseline design for SMD is an arrays of plastic scintillator strips. Strip size is 1cm-wide and 5mm-thick, and array of 12 strips covers one super-tower. Two orthogonal layers gives $\theta - \varphi$ position information with accuracy of better than 1 mm for e/γ of energy greater than several GeV. Ghosts are removed, though not completely, by pulse-height analysis.

Another shower position detector (SPD) is inststalled between EMC-1 and EMC-2. SPD has the same configuration as SMD. The purpose of SPD is to measure the direction of the isolated off-vertex photons. SPD also helps hadron shower position measurement by measureing early stage of hadron shower development, and thus improves track-cluster association for charged hadrons.

The baseline design has only one set of SPD. Whether we need more layers or not should be investigated.

12.2.4 Photon Detectors

Photon detectors for scintillating light are designed to sit at the end of the calorimeter assembly in the magnetic field, rather than stretching the clear fibers to the outside of the iron yoke of the whole detector. Therefore high-sensitivity photon detectors operational inside of 3 Tesla magnetic field are necessary. At present, we assume that;

- Both EMC and HCAL are read out by multi-channel HPDs;
- PSD are read out either by multi-channel HPDs or multi-channel HAPDs;
- SMD and SPD are read out either by multi-channel HAPDs or EBCCDs.

Here HPD, HAPD and EBCCD stand for Hybrid Photo-Diode, Hybrid Avalanche Photo-Diode, and Electron-Bambarded CCD, respectively. Though some fine-mesh photomultiplier tubes show quite high gain even in 2.5 Tesla, we decided not to use them. Detailed R&Ds are further needed to decide which option is better.

There are 133k , 20k, and 237k channels of EMC, HCAL, and SMD/PSD to read out, respectively. Therefore, it is impractical to use single-channel photon detectors. With multi-channel HPDs and EBCCDs under study at present, only one HPD and one EBCCD are necessary to read out of all the calorimetric signals and position detector signals of one super-tower, respectively.

12.2.5 Other Detector Options

There are several calorimter schemes other than the baseline-design tile/fiber scheme. The features of various detector schemes are summarized in Table 12.3. The features are potentials, and whether constructed detectors really have such features or not is a different question. For the energy resolution, resolution of typical EM calorimeters are quoted. Hadron energy resolution strongly depends on the detailed structure and analysis algorism. It should be stressed that longitudinal segmentation is essentially important for e/π separation.

Besides the properties in the table, liquid calorimeters have bad features as:

- Cryogenic pipes tend to behave as anomaly (or a hole at the worst case);
- Materials and gap between inside tracker and EMC deteriorates track-cluster association and EMC performance.

Nevertheless, liq.Ar calorimeter has been adopted by ATLAS detector due to its high resistance against radiation damage, which is not the case for LC environment. For large-scale general-purpose detectors at LC, therefore, tile/fiber scheme has the best-balanced features.

Detector Scheme	EM Energy Resolution	Transverse Segmentation	Longitudinal Segmentation	Hermeticity	Cost	Examples
Crystals	Excellent	Good	Poor	Good	Expensive	L3, Belle, CMS
SPACAL	Good	Good	Poor	Good	Expensive	H1, KLOE
Shashlik	Good	Good	Poor	Good	Expensive	Phenix, Hera-B
W/Si	Reasonable	Excellent	Excellent	Excellent	Tremendous	LUMs
liq.Ar	Good	Excellent	Excellent	Reasonable	Expensive	SLD, D0, H1, ATLAS
Tile/fiber	Reasonable	Reasonable	Excellent	Excellent	Reasonable	CDF, STAR

Table 12.3: Properties of various detector schemes for EM calorimetry.

12.3 Hardware Study

12.3.1 ZUES-type Test Module

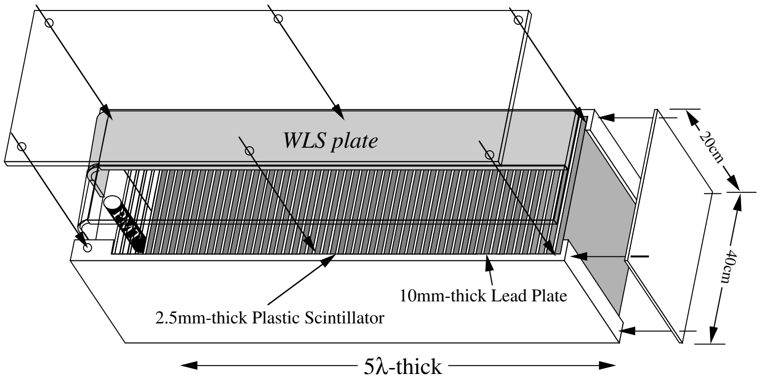

Figure 12.3: Schematical cut-away view of ZEUS-type test module.

We first investigated the possibility of ZEUS-type sandwich calorimeter because it was the best-operating hadron calorimeter in the collider detectors when we started R&Ds. Hadron calorimeter test modules were made with similar configuration to the ZEUS test modules [2]. It was composed of 10mm-thick lead plates and 2.5mm-thick plastic scintillator plates as shown in Fig. 12.3. This volume ratio was expected to acheive compensation. Photons were read out by WLS plates attached on the sides of the stack. Photon collection efficiency was higher than the tile/fiber scheme. Number of total layer was 80, which corresponds to the total thickness is $5\lambda_0$.

This simple structure realizes low-cost and easy assembling, but at the same time results in a massless gap.

Beam test was carried out at KEK $\pi 2$ beam line [3] using 1-4 GeV beams with a PSD, an SMD, and a SPACAL-type test module, which is described in the next section. Measured energy resolution is shown in Fig. 12.4. The results were as expected except the large constant term for pions, which was due to transverse shower leakage caused by small detector assembly cross section of 60cm×60cm. e/π ratio, a measure of compensation, was obtained to be 1.01. Also obtained was photo-electron yield of the module to be 160 p.e./GeV on average as shown in Fig. 12.5. This photo-statistics worsens the pion energy resolution from $40.0\%/\sqrt{E}$ to $40.8\%/\sqrt{E}$. This is not a problem for hadron calorimetry.

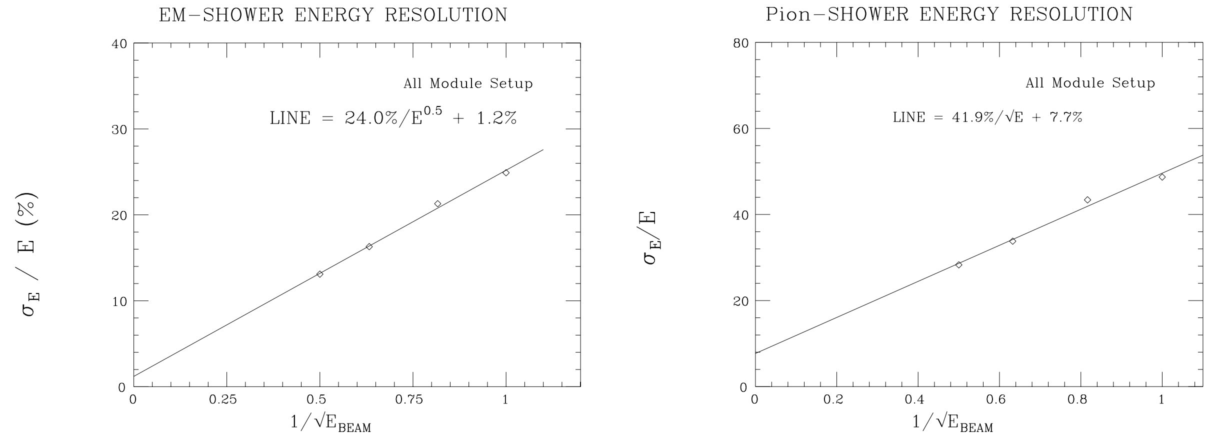

Figure 12.4: Energy resolutions of ZEUS-type hadron calorimeter test module for electrons (left) and for pions (right).

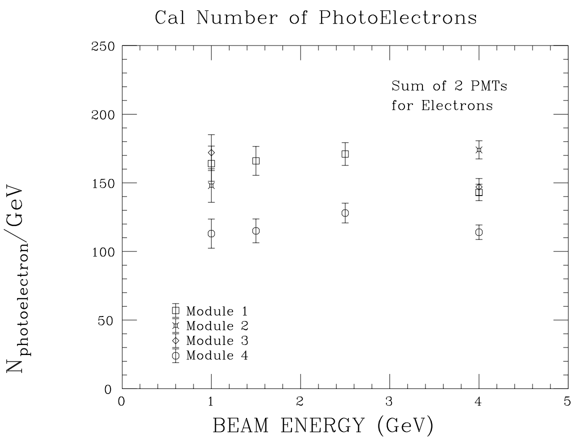

Figure 12.5: Photo-electron yield of ZEUS-type hadron calorimeter test module for electrons. The same amount is expected for pions since the module was hardware-compensating.

In order to test the response to electrons, another ZEUS-type EM calorimeter test module was made with 4mm-thick lead plates and 1mm-thick plastic scintillator plates. Beam test was carried out at KEK $\pi 2$ with 1-4 GeV beams. Measured energy resolution and photo-electron yield are shown in Fig. 12.6. Obtained energy resolution of $15.4\%/\sqrt{E} \oplus 0.2\%$ satisfies expected resolution. The measured photo-electron yield of 660 p.e./GeV has effect on the stochastic term of the energy resolution to worsen it

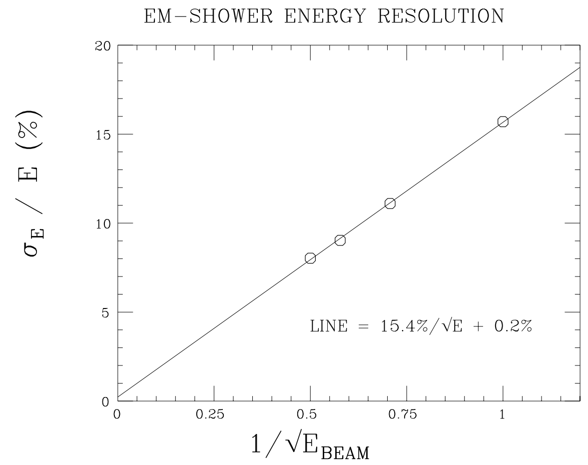

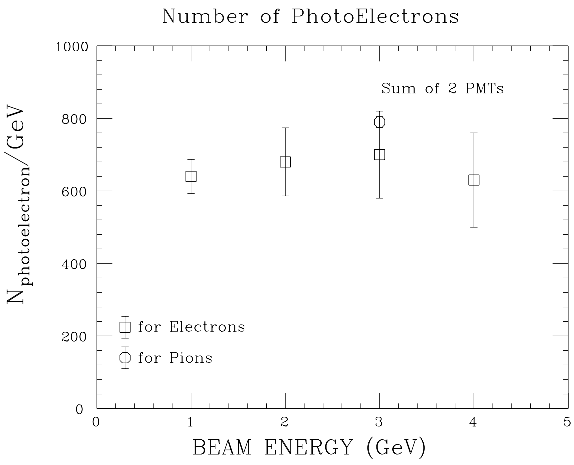

Figure 12.6: Energy resolution (left) and photo-electron yield (right) of ZEUS-type EM test module.

from $15.0\%/\sqrt{E}$ to $15.5\%/\sqrt{E}$. This is not negligible, and photon readout scheme with better photon collection efficiency shoule be desirable at least for the EM calorimeter.

Though measured energy resolutions were quite satisfactory, we decided not to continue R&Ds of ZEUS-type sandwich calorimeter due to following reasons:

- Longitudinal segmentation is difficult;
- Massless gap made by WLS plates running radially introduces signigficant response anomaly.

12.3.2 SPACAL-type test module

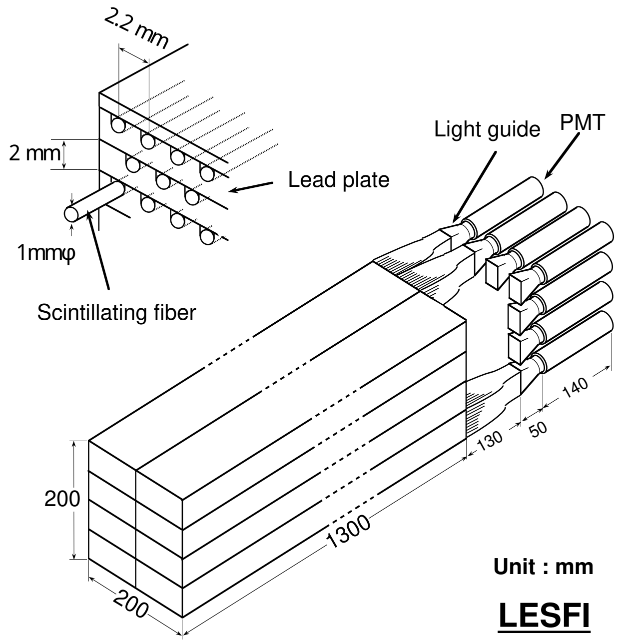

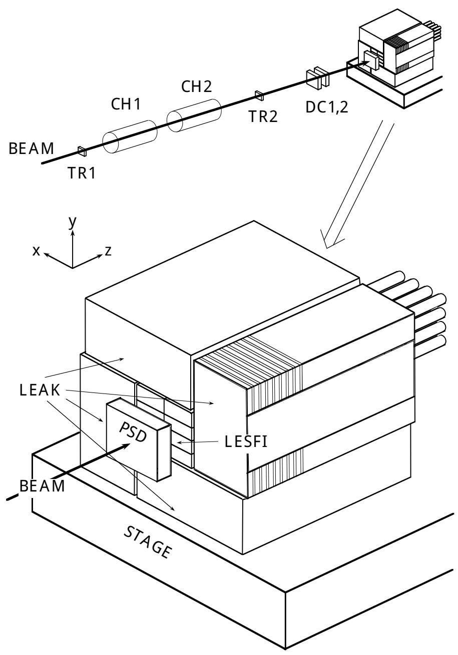

Figure 12.7: Schematical drawing of the SPACAL-type test module (left) and setup of the combined beam test of ZEUS-type and SPACAL-type test modules at KEK-π2 beamline (right).

We also studied SPACAL-type calorimeter in parallel with the ZEUS-type calorimeter at the first stage of the R&D because the SPACAL-type calorimeter was the best-performance calorimeter that time, even though there was no running experiment using SPACAL. Since SPACAL-type calorimeter is quite expensive and extremely elaborating, we built only one module with sizes of 20cm×20cm×130cm as shown in Fig. 12.7. Pure lead plates with grooves are stacked, and 1 mmϕ scintillating fibers are embedded in the grooves. The volume ratio of lead to scintillator is 4:1 for hardware compensation. One module was read out by 16 PMTs to have 4×4 sub-tower structure for transverse shower profile measurement.

Beam test was done at KEK $\pi 2$ beamline using 1-4 GeV beams [3]. The setup is also shown schematically in Fig. 12.7. One SPACAL-type module at the center was surrounded by the ZEUS-type calorimeter modules, and a PSD was set in front of the SPACAL for some measurements.

Measured energy resolutions are shown in Fig. 12.8. The results are parametrized as

$$\frac{\sigma_E}{E} = \frac{(14.4 \pm 0.3)\ \%}{\sqrt{E(\mathrm{GeV})}} \oplus (0.0 \pm 1.4)\ \% \quad \text{for electrons,}$$

$$\frac{\sigma_E}{E} = \frac{(38.1 \pm 1.3)\ \%}{\sqrt{E(\mathrm{GeV})}} \oplus (11.6 \pm 1.4)\ \% \quad \text{for pions.}$$

These resolutions were very good except the large constant term due to transverse shower leakage. We also obtained pion rejection factor of 1/200 with electron efficiency of 98% using PSD pulse height and transverse shower profile. This rejection score is not very high because it is difficult to separate e/π with transverse shower profile at low energies ; longitudinal profile does better.

In conclusion of the series of R&Ds, we decided not to continue R&Ds of SPACAL-type calorimeter due to following reasons:

- Longitudinal segmentation is very difficult;
- Preshower and shower-max detectors can not be integrated naturally;
- Really expensive and elaborating.

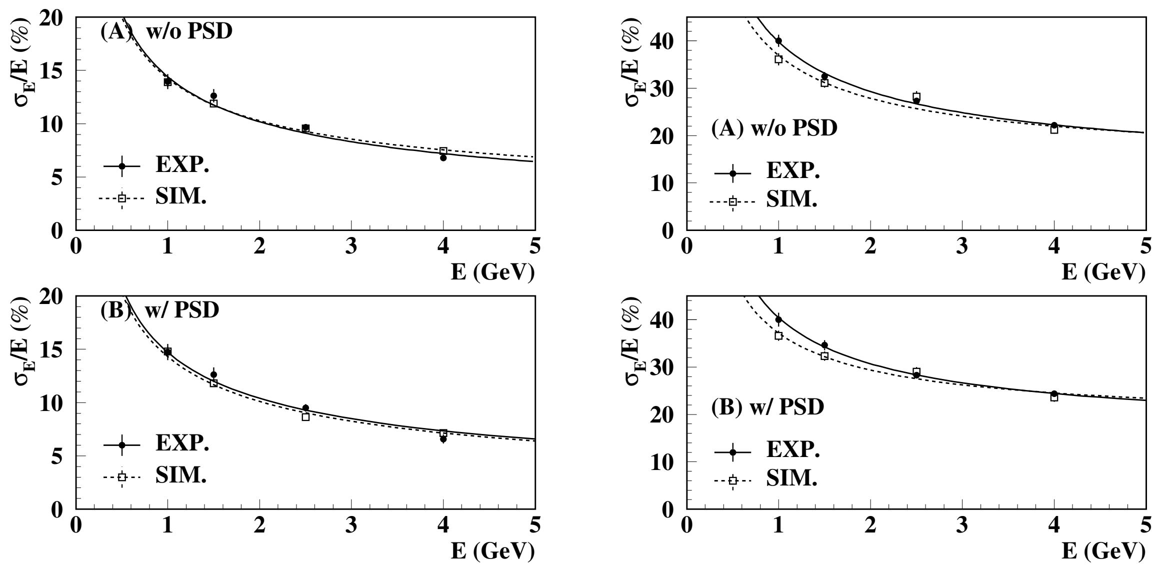

Figure 12.8: Energy resolutions of SPACAL-type test module for electrons (left) and for pions (right). Bottom figures are for measurements with PSD in front, and top ones are without PSD. Dotted lines are results of GEANT simulation.

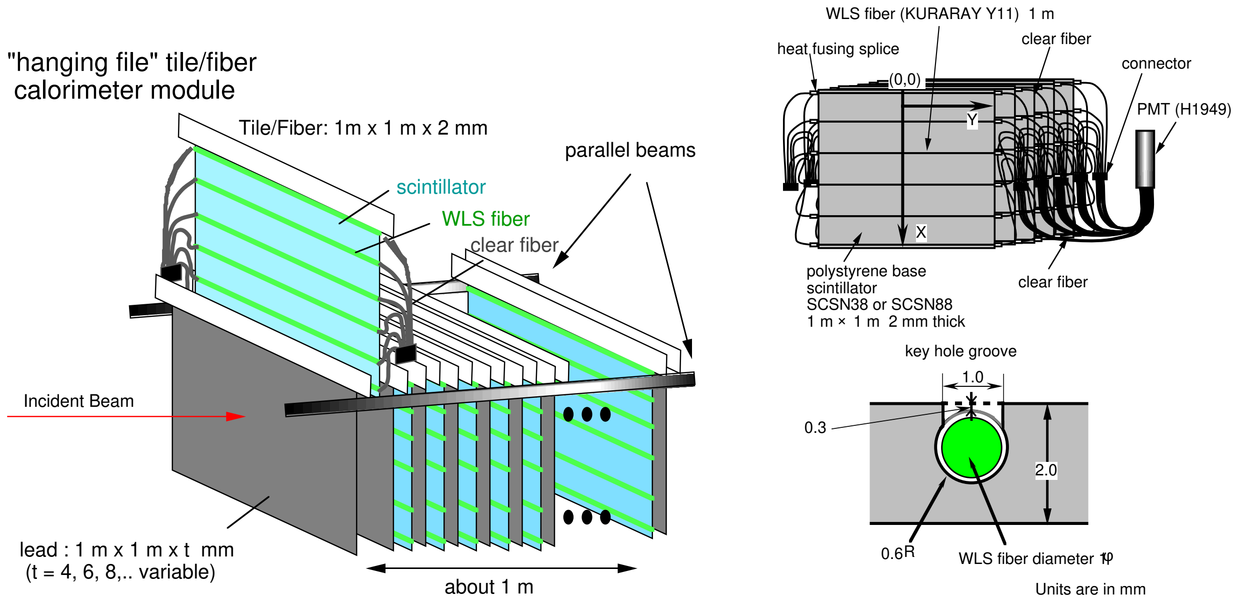

Figure 12.9: Schematical view of straight-groove hanging-file test module (left), and optical readout scheme (right).

12.3.3 Tile/Fiber Test Module

Tile/fiber structure is characterized by a wavelength shifting (WLS) fiber embedded in a plastic scintillator tile. This enables compact optics for light transfer from scintillators to photon detectors without sacrificing photon yield so much. This scheme was extensively studied by SDC group, and then by CDF group with slightly different fiber layout. The tile/fiber calorimeters have been widely adopted by CDF, STAR, CMS, and so on. For the JLC calorimeter, the tile/fiber sturcture with hardware compensation was adopted as a revised baseline design in 1996, and systematic R&Ds were initiated. Following bench tests of each component, test modules were constructed for generic shower study and realistic performance study, and series of beam tests were carried out at KEK and at FNAL. In the following sections, detail of the R&Ds are described.

1) Generic Studies with Straight-groove Module

Though extensive R&Ds had been carried out by SDC/CDF group before 1996, combination with hardware compensation raised tow open questions:

- First of all, possibility of hardware compensation itself with tile/fiber configuration must have been established. There were several calculations and measurements on compensation with lead and plastic scintillator sampling calorimeters[3, 4, 5]. However those results had significant discrepancies with each other. Addition of fiber-routing plates for tile/fiber configuration was another unknown factor on compensation. This might affect the compensation condition. Those problems must have been examined before making calorimeter module of tile/fiber design.

- In order to realize required energy resolution with hardware-compensating composition using lead absorber, very thin scintillator plates of 1mm-thickness should be used for EM calorimeter, and 2mm for hadron calorimeter. Photon yield, uniformity, and mechanical feasibility must have been examined for such thin sciltillator plates.

A test module with hanging-file structure was constructed to examine possibility of hardware compensation. The structure is schematically shown in Fig. 12.9. Lead plates and scntillator plates, and acryl plates if necessary, were hung over a pair of supporting beams to enable re-configuration for generic studies. As absorbers, 4mm-thick lead plates and 2mm-thick lead sheets were used to change the lead

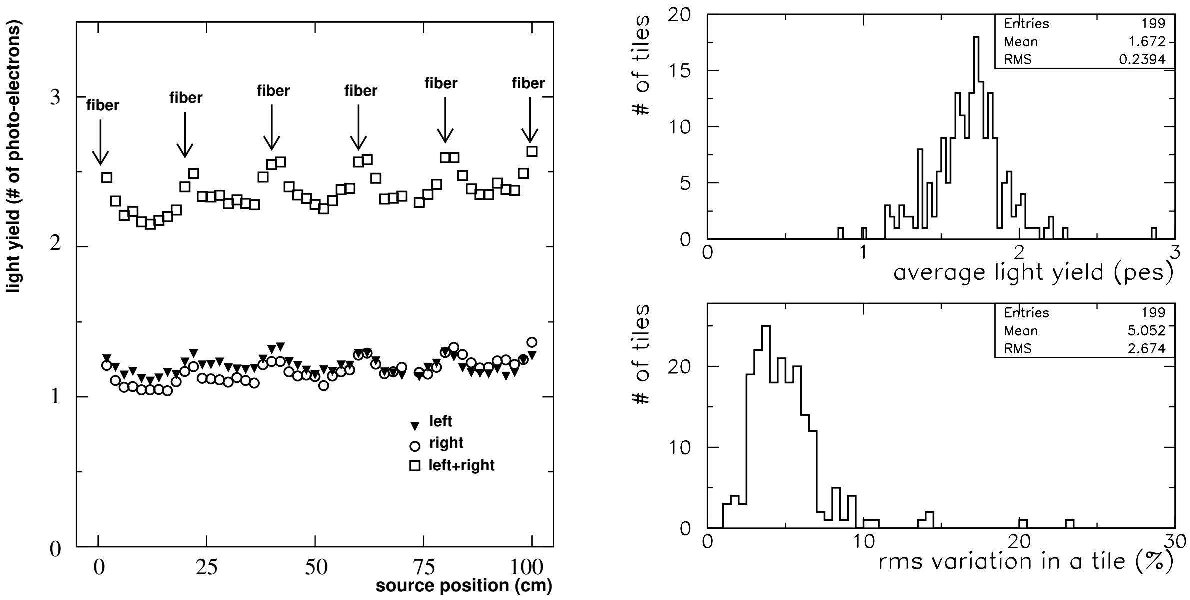

Figure 12.10: Non-uniformity of photo-electron yield over one scintillator plate (left), distributions of its average (right-top) and RMS (right-bottom).

thickness from 4 mm to 16 mm by 2mm-step. The thicknesses of plastic scintillator plates and acryl plates, on the other hand, were fixed to be 2 mm. Transverse size of the plates were 1m$\times$1m for good shower containment.

Photon-readout scheme is also shown in Fig. 12.9. The scintillator plates had six straight grooves of key-hole cross section, where 1 mmϕ WLS fibers were embedded. Distance between the grooves, 20cm, was determined to re-use the scintillator plates for the tile/fiber module. Fibers from five successive scintilator plates on each side were ganged to form a superlayer, and were read out by one PMT. There were 42 superlayers in the configuration with 4mm-thick lead plates, and detailed study on longitudinal shower profile was carried out. In the case of 8mm-thick lead plates, there were 24 superlayers, resulting in the total thickness of $6\lambda_0$.

Response of scintillator plates were measured with an RI source before assembling. Non-uniformity of photo-electron yield over one scintillator plate and distributions of its average and RMS are shown in Fig. 12.10. Since the fiber distance is rather large, average photo-electron yield is only 1.6 p.e./MIP. Measured response map shows prominent peaks at the embedded WLS locations. Effects of measured non-uniformity and distribution of average photo-electron yield on calorimeter responses were examined by GEANT simulation, and concluded not to be significant for hadrons [6].

Energy Measurement

Series of beam tests were carried out at KEK $\pi 2$ beam line with beam energies from 1 GeV to 4 GeV [6]. Fig. 12.11 shows energy resolution for pions and e/π response ratio versus lead plate thickness. Target energy resolution is achieved with lead plates of 8mm-thick or thinner. The hadron energy resolution of $33.6\%/\sqrt{E}$ achieved with 4mm-thick lead plates are one of the best hadron energy resolution achieved so far. In Fig. 12.11, dependence of energy resolution on lead thickness is parametrized as $\sigma_E = \sqrt{\sigma^2_{intrinsic} + (\sigma^2_{sampling} + \sigma^2_{photostat}})$, neglecting the constant term. Fitting was done and intrinsic hadron shower fluctuation was obtained to be 24.4$\pm$0.7%. This is significantly larger than previously reported value of 13.4$\pm$4.7% by ZEUS [7]. This could be due to the difference of incident energy.

Hardware compensation should be achieved with 9mm-thick lead plates in the case of 2mm-thick plastic scintillator plates.

In order to check effect of fiber-routing acryl plates on compensation, three configurations are tested in the case of 8mm-thick and 16mm-thick lead plate configurations:

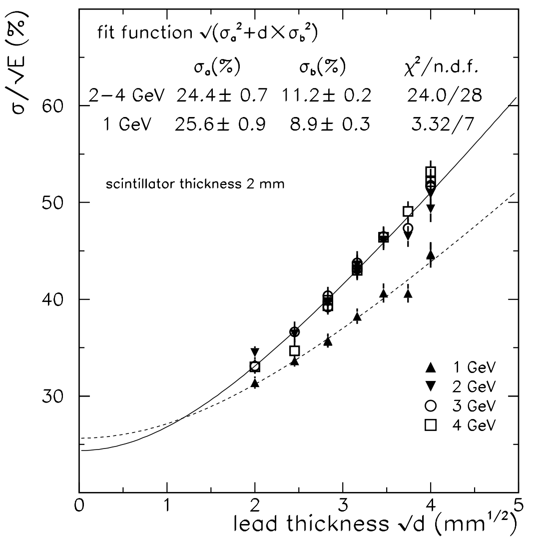

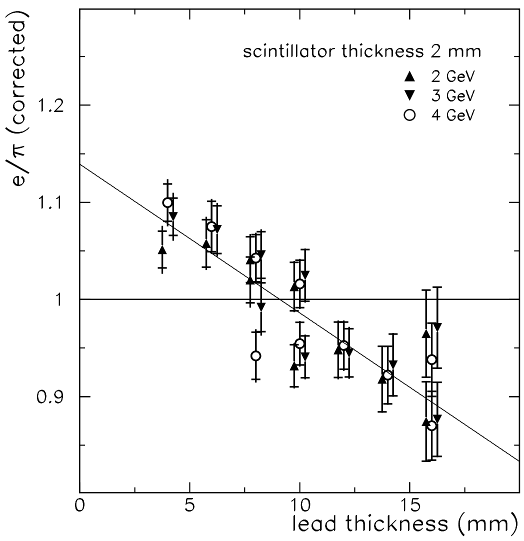

Figure 12.11: Energy resolution for pions (left) and e/π ratio (right).

- no acryl plates were used (lead and scintilator only);
- an acryl plate was put upstream-side of every scintillator plate;
- an acryl plate was put downstream-side of every scintillator plate.

The motivation of measurement with 16mm-thick lead plates was such that compensation might be achieved with 16mm-thick lead plates + 2mm-thick scintillator plates + 2mm-thick acryl plates, resulting in the volume ratio of lead to total plastic to be 4:1. Effects of acryl plates on the energy resolution and e/π ratio is summarized in Table 12.4 for 8mm-thick case. It is seen that acryl plates does not destroy the hardware compensation if they are placed downstream-side of scintillator plates. Hadron energy resolution, however, gets slightly worse by their presence regardless of their location.

	σ_E/E for electrons	σ_E/E for pions	e/π ratio
No acryl plates	(12.0±0.5)%	(20.5±0.4)%	1.03±0.02
Acryl plates upstream	(11.6±0.5)%	(22.7±0.4)%	1.07±0.02
Acryl plates downstream	(12.0±0.5)%	(22.8±0.4)%	1.01±0.02

Table 12.4: Energy resolutions and e/π ratios with and without acryl plates for 4 GeV/c electrons and pions in the case of 8mm-thick lead plate configuration.

Shower Fluctuation Analysis

Longitudinal shower profile and its event-by-event fluctuation was studied with configuration of 4mm-thick lead plates, which had 42 longitudinal samplings (superlayers). The purpose of this study is;

- Improve hadron energy resolution (software weighting);
- Construct parametric hadron shower generator with realistic fluctuation;
- Obtain e/π separation capability as a function of the longitudinal segmentation of the calorimeter.

Analysis has been done for both EM and hadron showers following the work by CDF for EM shower analysis[8]. Correlation between pulsehieght fluctuations for different superlayers are shown in Fig. 12.12 for raw fluctuations δ_i and for orthogonalized fluctuations $\tilde{\delta}_i$. Orthogonalization is done by diagonalizing

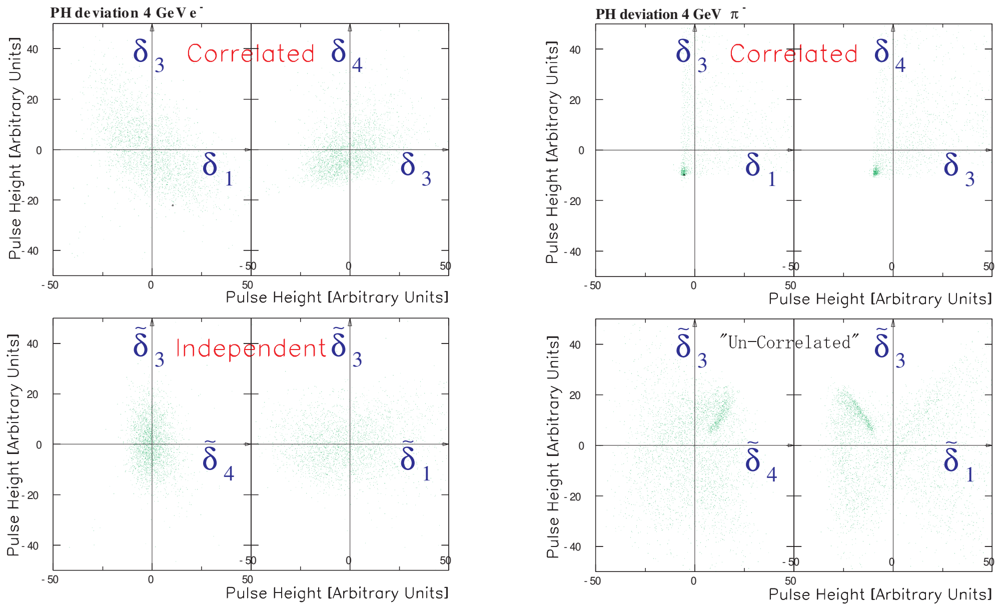

Figure 12.12: Correlation between pulsehieght fluctuations for different superlayers for electrons (left) and for pions (right). Top distributions are for raw fluctuations, and bottom ones are after orthogonalization.

correlation matrix of raw fluctuation, and obtaining the eigen vectors. In the case of electrons, no correlation is seen between amplitudes of the orthogonalized eigen vectors. On the other hand, $\tilde{\delta}_i$ for pions have correlation even after orthogonalization procedure, and orthogonalization of hadronic fluctuation is not yet successful. Therefore parametrization of hadron shower fluctuations with orthogonal parameter set has not been completed yet.

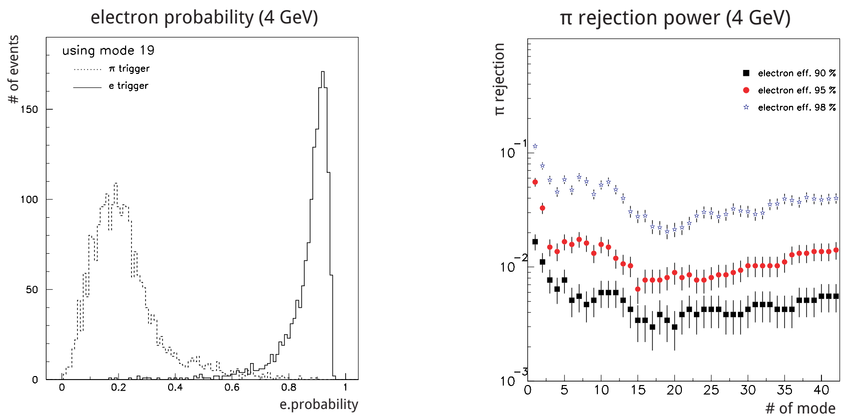

Figure 12.13: e/π separation by pulseheight fluctuation from template distributions for electrons and pions. Left histogram is electron probability distribution for electron and pion samples, and right plot is pion rejection factor as a function of number of modes (used eigen vectors).

Pulseheight fluctuation can be used to improve e/π identification, which is usually done by shower profile only. Deviations of measured pulseheights from electron profile template and from pion profile template are normalized by typical fluctuation for each particle, and likelihood to each particle are calculated. Distribution of electron-ness and pion rejection capability are shown in Fig. 12.13. Number of mode in the bottom figure is number of eigen vectors of pulseheight fluctuation used in the analysis. Since there are 42 superlayers, there are 42 orthogonal eigen vectors to represent pulseheight fluctuation. Using six or seven major eigen vectors achieves almost the best score ; higher minor eigen vectors are noisy, and using them does not improve the score. For single-particle e/π separation, therefore, six longitudinal segmentation should be good enough if they are segmented in optimum way.

2) Study of Tile/Fiber Module

Based on the results of the generic studies and tile bench tests, the straight-groove module was rebuilt to be a tile/fiber calorimeter module. The design of the module is schematically shown in Fig. 12.14. The module was composed of a front section (FCAL) and a rear section (RCAL).

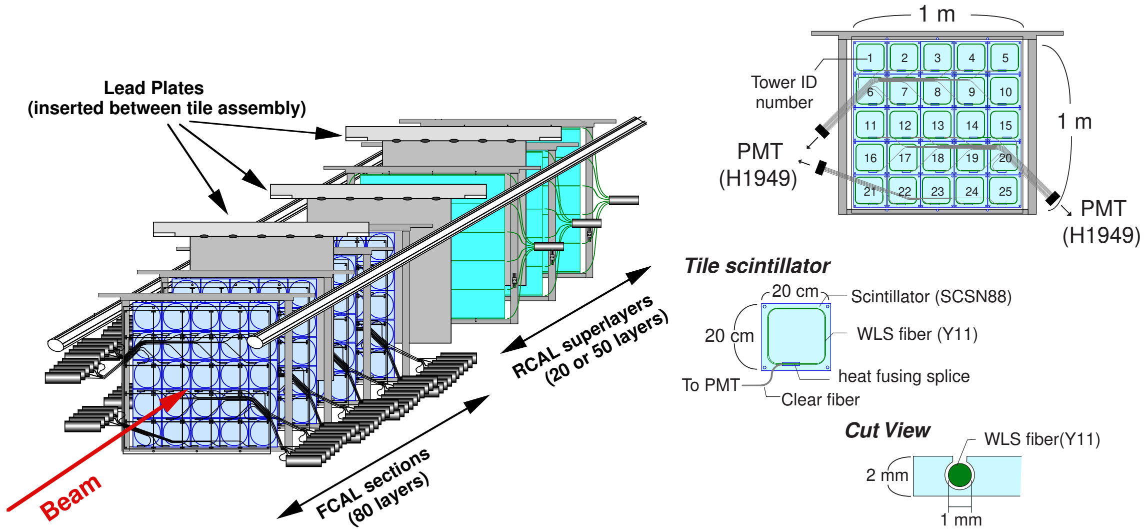

Figure 12.14: Schematic view of the tile/fiber test module (left) and layout of fibers and tiles (right).

In the FCAL part, the 1m×1m plastic scintillator plate was modified to be a scintillator tile assembly as shown in Fig. 12.14. Twenty-five tiles with size of 20cm×20cm×2mm-thick were arranged on a fiber-routing acryl plate to form 5×5 tower structure. Four sides of the tiles were painted white with TiO_2-based emulsion, and were covered with white PET films for better light collection efficiency. The tile had a σ-shaped groove with a key-hole cross section, where a WLS fiber is embedded. The WLS fiber was connected to a clear fiber by heat splicing at the exit from the tile. The clear fiber ran in the groove on the fiber-routing acryl plate to exit from the detector, and was connected to a photon detector. Photo-electron yield and uniformity over a tile measured with β rays from an RI source are shown in Fig. 12.15 Obtained photoelectron yield is translated to the calorimeter response of 83 p.e./GeV for 8:2 configuration. This slightly worsens the stochastic term of hadron energy resolution from $40\%/\sqrt{E}$ to $41\%/\sqrt{E}$, which is not a problem for hadron calorimetry. The measured non-uniformity was estimated using GEANT3 simulation to introduce systematic uncertainty of 0.3% on average on energy resolution measurement. This, again, is not significant.

These tile assemblies were interleaved with 8mm-thick lead plates. There were 80 layers of the tile assemblies in FCAL in total. They were divided into four sections longitudinally, each of which contained 20 layers. One quadrant of a tower were read out by one PMT.

Following the tile/fiber part, unmodified straight-groove section remained as RCAL. There were two superlayers in RCAL in the case of low energy beam test at KEK. In the case of high energy beam test at FNAL, ten superlayers were installed, the last of which did not have lead absorbers to be used for muon tagging. RCAL also had 8mm-thick lead plates as absober.

The layouts of the beam tests at KEK and at FNAL are schematically shown in Fig. 12.16. Both setups are quite similar except for that there were momentum-analyzing devices at FNAL beam test, and that SRD was used for electron identification at FNAL instead of Cerenkov counters. Details of the setup and analysis are given elsewhere [6, 9]. Energy of the beam was 1-4 GeV and 10-200 GeV at KEK and at FNAL, respectively. The beam was unseparated, and particle identification was done off-line. In the case of FNAL test, however, electorn-rich and pion-rich conditions were realized by

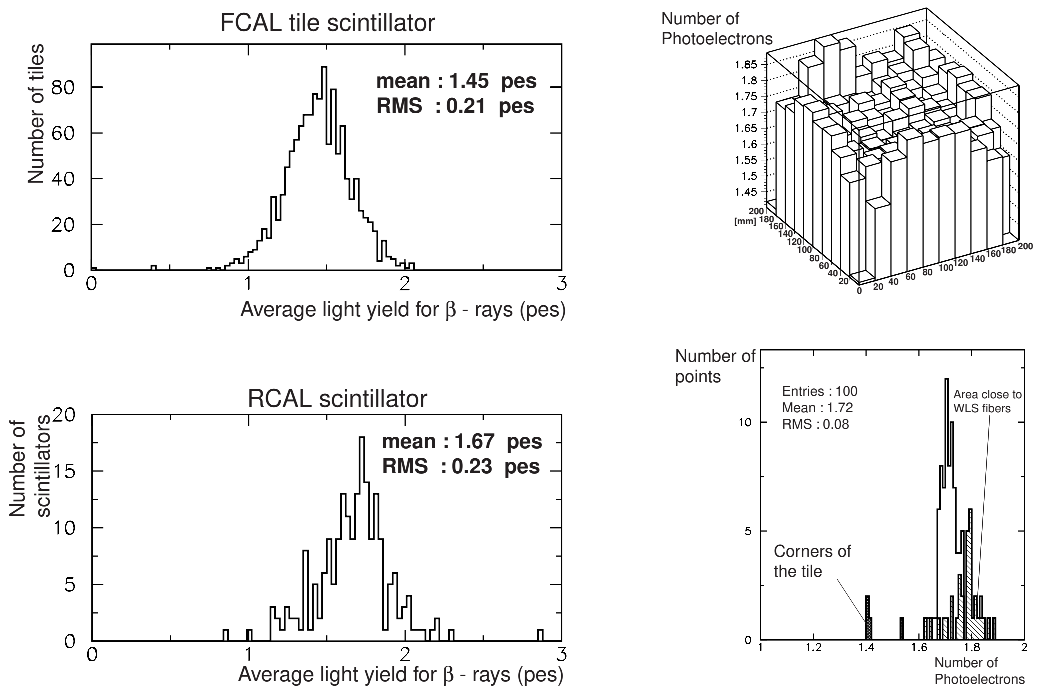

Figure 12.15: Average photo-electron yield for tiles (left-top), average photo-electron yield for straight-groove plates (left-bottom), uniformity over one tile (right-top), and distribtion of photo-electron yield for a tile (right-bottom).

selecting appropriate converters/absorbers on the beamline. Tower-to-tower gain calibration was done using penetrating muons.

Energy Measurement

Measured energy resolution, linearity, and e/π ratio are shown in Figs. 12.17 and 12.18. The energy resoltion is slightly worse than those shown in Fig. 12.11, and is consistent with that of the straight-groove module with acryl plates interleaved shown in the Table 12.4. We can therefore conclude that acryl plates used for fiber-routing do deteriorate the energy resolution, regardless their location. On the other hand, the e/π ratio is consistent with 1.0, and hardware compensation is established to be retained in the case of the tile/fiber structure if each acryl plate is located downstream-side of each scintillator assembly.

If we stick to the hadron energy resolution of $40\%/\sqrt{E}$, sampling frequency of the HCAL should be finer than 8mm-thick lead plates plus 2mm-thick plastic scintillator. However measred hadron energy

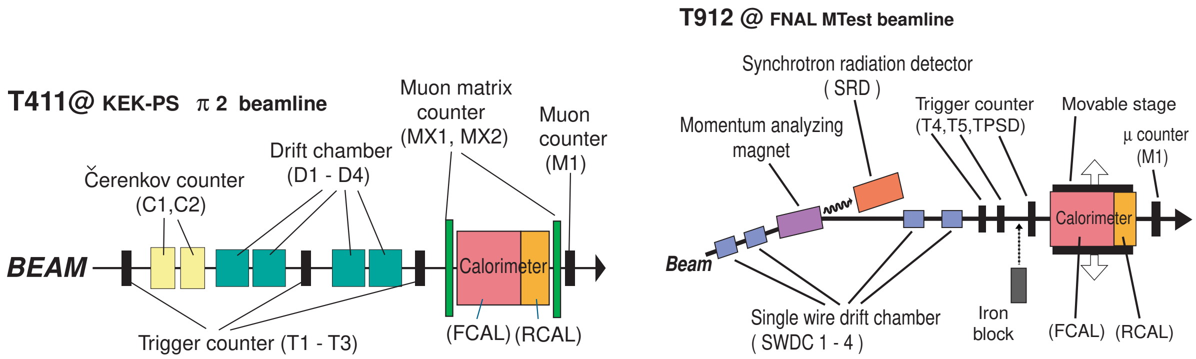

Figure 12.16: Setup of the beam test at KEK (left) and at FNAL (right).

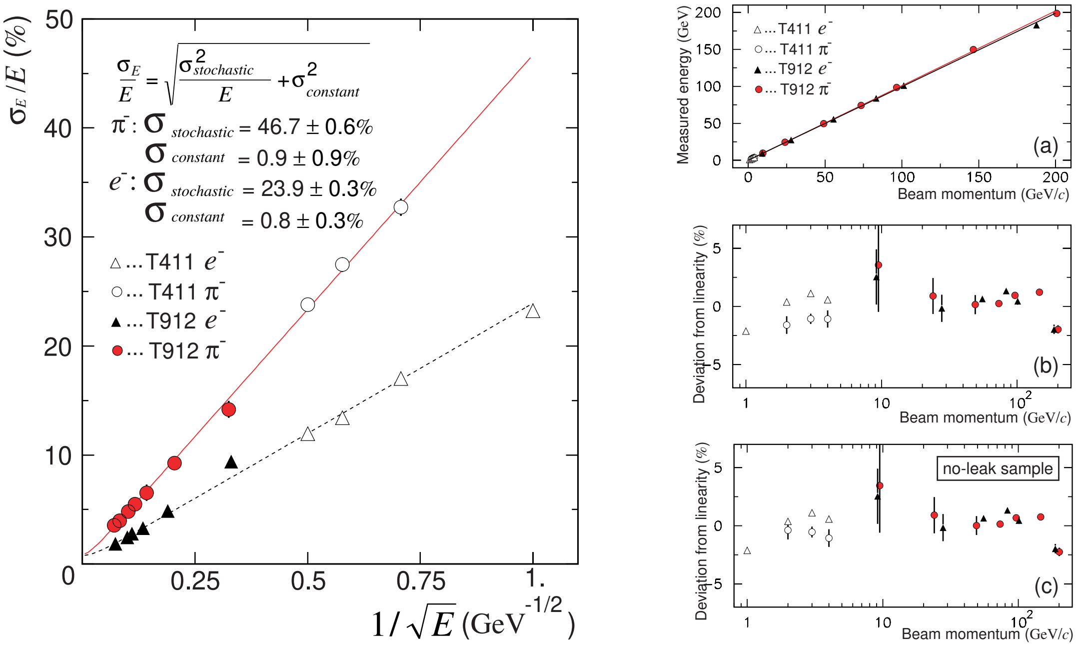

Figure 12.17: Energy resolution (left) and linearity (right) of the tile/fiber test module.

resolution of $46\%/\sqrt{E}$ may be acceptable for physics analysis. This should be examined by further simulation study.

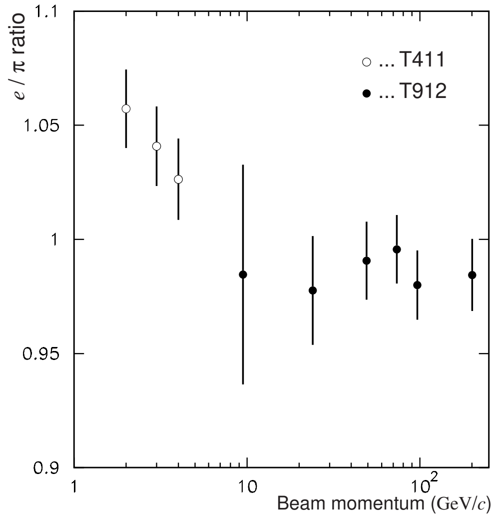

Figure 12.18: e/π response ratio of the tile/fiber test module.

Tower Property

Cross-talk between towers measured with electron central injection are shown in Fig. 12.19. Amount of cross talk to adjucent towers are 1%-level. This is consistent with the optical crosstalk at the bench test measured with an RI-source. Cross talk of this level is negligible to hadron shower analysis. For EMC of finer-granularity option, however, cross talk may have significant impact, and needs to be examined.

Response at the tower boundary are shown in Fig. 12.20. Energy measurement for pions may have enhancement of about 3% at the region where WLS fibers are embedded. This is consistent to the non-

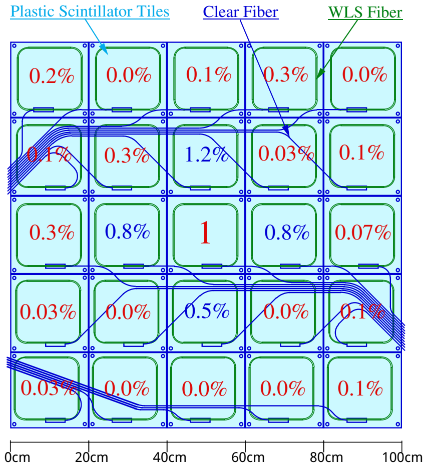

Figure 12.19: Cross talk between towers for the tile/fiber test module.

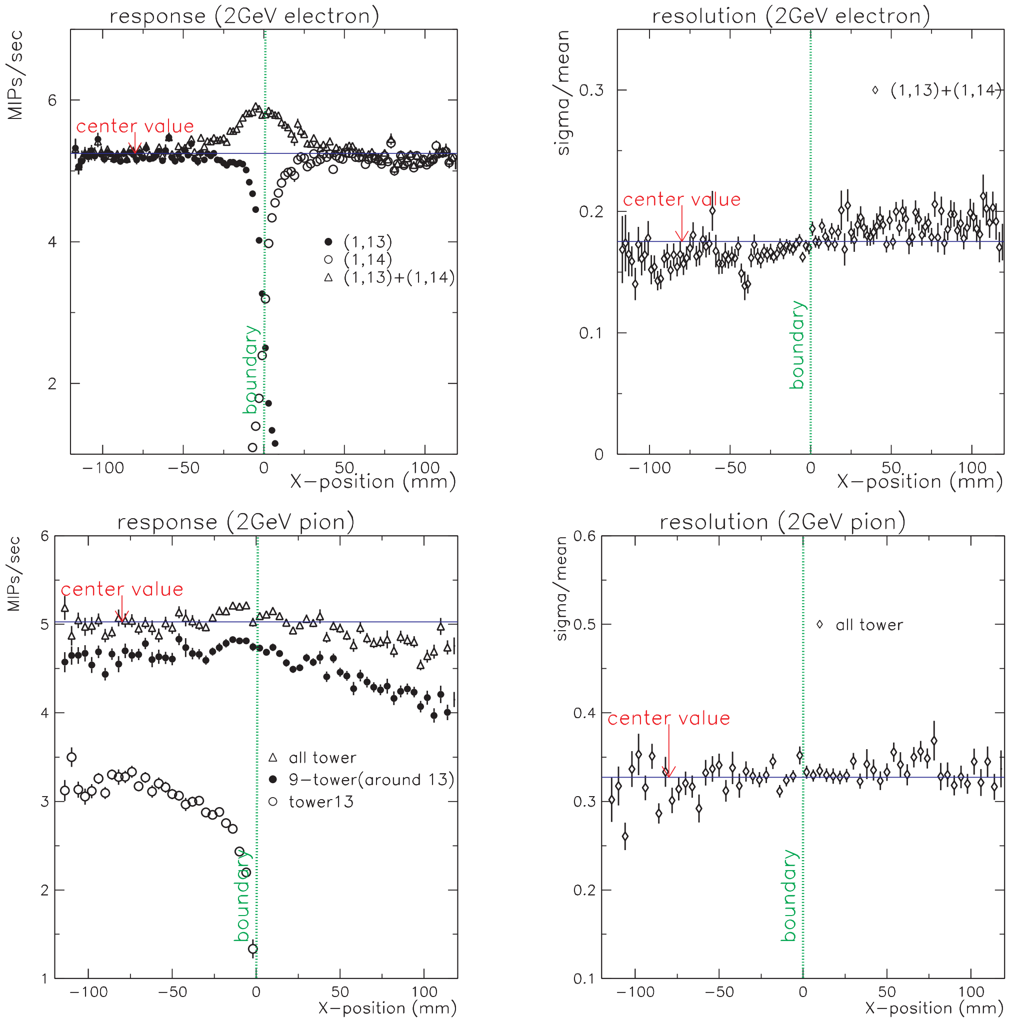

Figure 12.20: Tower boundary response of the tile/fiber test module. Top figures are responses for electrons, and bottom ones are for pions. Left figures are energy measurement, while right ones are energy resolutions.

uniformity at the bench test shown in Fig. 12.15. This enhancement is not significant when EMC is loacted before the HCAL and response smears out. On the other hand, energy measurement for electrons has prominent enhancement at the boundary. This must be equalized by ajusting reflection index of tile surface around the WLS when EM modules are constructed.

EMC study

Photo-electron yield of 1mm-thick scintillator for EM calorimeter was measured for 10cm×10cm tiles. It also had a σ-groove, and 0.7 mmϕ WLS fiber was used. The average photo-electron yield was obtained to be three as shown in Fig. 12.21. This corresponds to 350 p.e./GeV for compensating calorimeter, and is not sufficient for EM calorimetry. Comparison between 20cm×20cm×2mm-thick tiles and 10cm×10cm×1mm-thick tiles suggests that photo-electron yiled is inversely proportional to the area of tiles, since we know from independent measurement that photo-electgron yiled is proportional to the tile thickness. Smaller tiles such as 5cm×5cm is considered to have sufficient photo-electgron yiled. This, together with non-uniformity, should be established by further measurement.

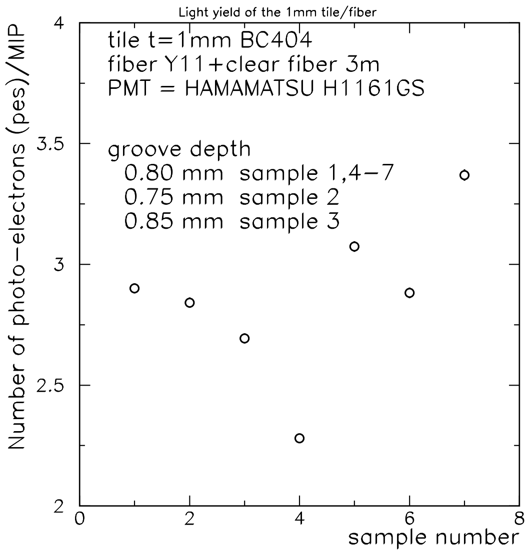

Figure 12.21: Photo-electron yield of 10cm×10cm×1mm-thick tiles.

R&Ds on another option of finer-granulartiy EMC, made of stacks of scintillator strip arrays like SMD, are in progress. This option requires huge number of photo-detector channels, and has become possible by recent advances in multi-channel HPD or EBCCD. Whether we can remove ghosts efficiently or not must be investigated with a full simulator.

Bench tests on strip properties were carried out for various strip sizes with thickness of 2 mm. Non-uniformty of photo-electron yield over a strip was measured to be 4.8% at most for 1cm-wide strips, and is acceptable for EMC. Average photo-electron yield, on the other hand, is 4.6 p.e./MIP. This corresponds to 260 p.e./GeV in the case of compensating EMC, and needs further improvement. However, if software compensation is possible even with the orthogonal $\theta - \varphi$ scheme, thicker strips can be used, and photo-electron yield will not be a problem. Detailed full simulation studies are again needed to examine apllicability of software compensation for this scheme.

12.3.4 Preshower and Shower-max detectors

The purpose of PSD and SMD are to identify $e/\pi^{\pm}/\gamma/\pi^0$, and improve cluster separation and track-cluster association. For this purpose, fine segmentation is necessary for SMD. First we studied SMD of Si-pad array as the HES of ZEUS. Test modules were made with Si-pad array firstly with pad size of

1cm×1.5cm and array size of 18×12, then secondly with pad size of 1cm×1cm and array size of 16×16 with improved readout electronics. Beam tests were carried out in combination with PSD and hadron calorimeter modules[10].

Later on, we moved to the scintillator-strip option since:

- Si-pad SMD was thought to cost too much;
- Scintillator-strip SMD used the same technique as the tile/fiber calorimter, and was easily integrated with calorimeter.

Since the baseline JLC calorimeter size is now much smaller than the previous one, the first reason may be no more true. However re-examination of the possibility of Si-pad option has not yet started.

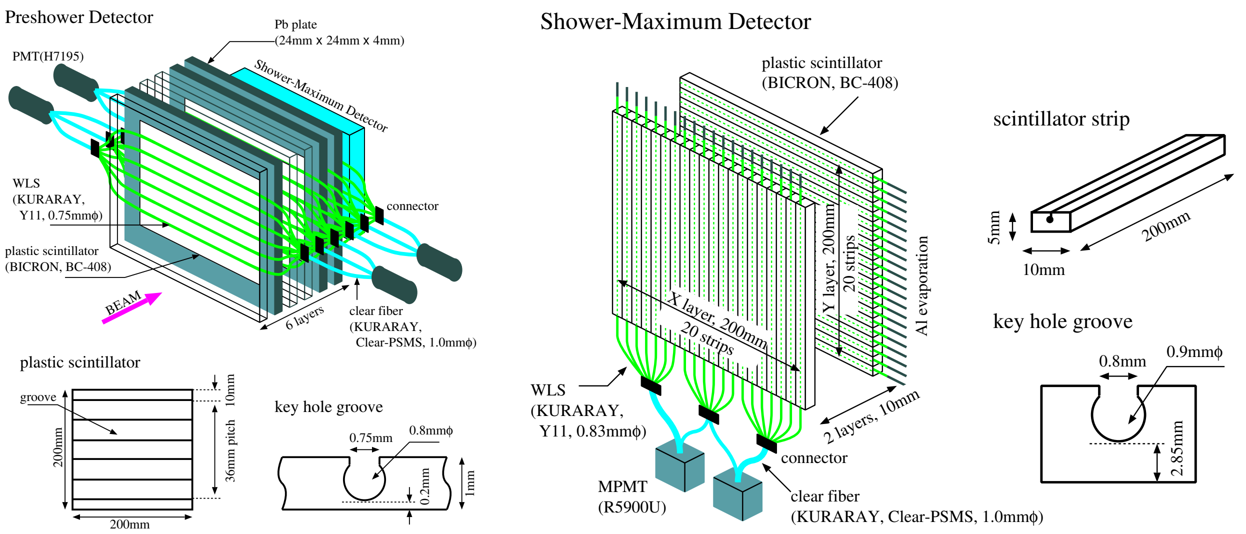

Figure 12.22: Schematical drawing of PSD (left) and SMD (right).

According the the baseline design, we built test modules of PSD and SMD, and carried out a beam test at FNAL in combination with the tile/fiber hadron calorimeter [11]. The designs of PSD and SMD modules are schematically shown in Fig. 12.22. Photons from scintillators are read out by WLS fiber assembly in both PSD and SMD. In the case of SMD, fibers are connected to multi-channel PMTs, and each strip is read out separately.

In order to separate electrons from pions, three variables are defined:

- S is a measure of lateral shower spread defined as $S = \sqrt{\sum_i d_i^2 E_i / E_{tot}}$
- D is a measure of longitudinal shower depth defined as $D = \sum_j z_j E_j / E_{tot}$
- R is a ratio of energy in PSD to total energy.

Examples of e/π separation capability of S and D variables are shown in in Fig. 12.23. It is seen that D-variable has excellent performance in e/π separation, and thus that longitudinal segmentation is quite important. Measured e/π separation capabilities are shown in Fig. 12.24 and summarized in Table 12.5. Obtained score of mostly bettern than 1/1000 are comparable to other measurements [12], and is satisfactory.

Hit multiplicity of SMD can also be used to identify electrons. By requiring more than 10 hit-strips out of 40 strips, pion rejection factor of about 10 can be achieved with electron efficiency of 98%. However this has strong correlation with R-value, and is not included in the table 12.5.

Measured position resolution is shown in Fig. 12.25. Present result is much worse than the baseline requirement of better than 1 mm for energies higher than several GeV. The is due to saturation and cross talk of PMTs, and should be solved before going to the next step.

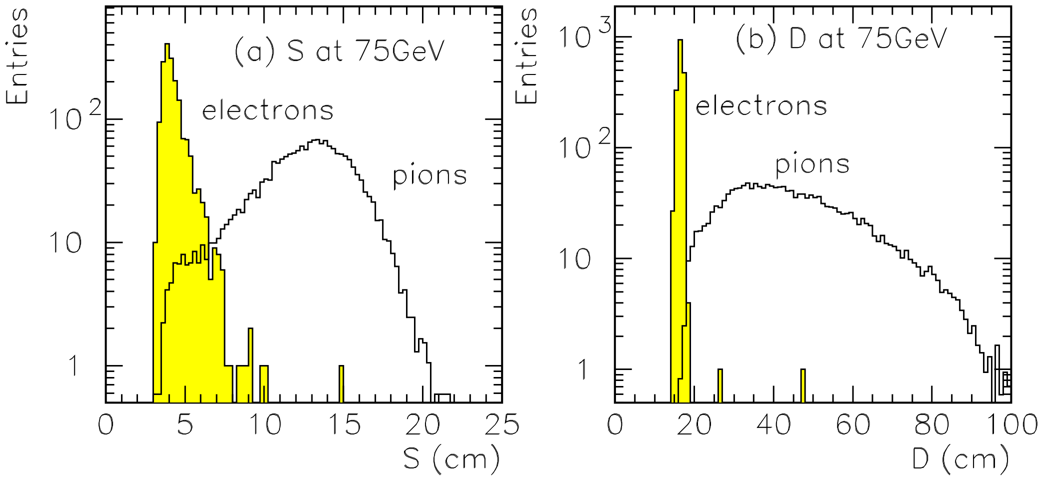

Figure 12.23: e/π separation capability of S-variable (left) and D-variable (right).

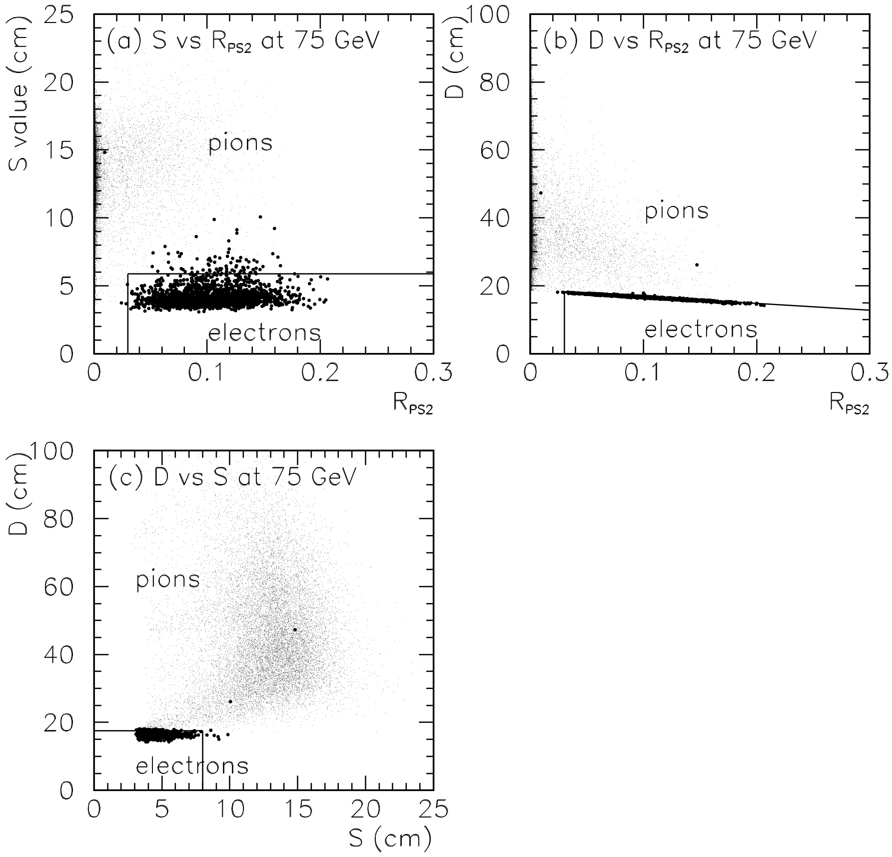

Figure 12.24: e/π separation capabilities using combinations of S, D, and R variables..

Method	S value and R_{PS2}			D value and R_{PS2}			D and S values		
ϵ_e (%)	90	95	98	90	95	98	90	95	98
r_π at 50 GeV	473	312	180	1274	1104	720	1183	828	753
r_π at 75 GeV	657	487	343	1258	1162	944	1510	1162	888
r_π at 100 GeV	984	656	281	1640	1406	1406	984	820	656

Table 12.5: Pion rejection factors with the combinations of R_{PS2}, S and D values.

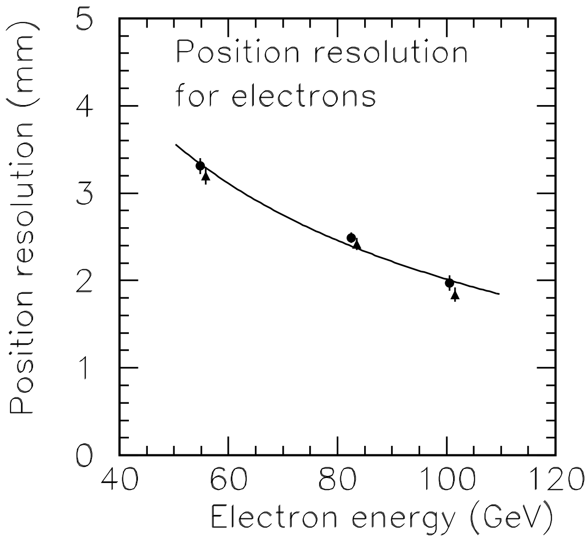

Figure 12.25: Position resolution of SMD.

The WLS fiber assembly costs significant amount of the total cost of scintillator-array SMD. In order to reduce the total cost of SMD, an option which use photo-diodes (PDs) instead of WLS fiber assembly are being studied. Silicon PIN PDs or APDs are attached at the both end of the strips, and photons are directly read out by the PDs. Direct punch-through of charged partilces will be identified by double-layer scheme; a blind PD is pasted behind the detector PD.

Studies so far indicates that PIN PDs do not have enough sensitivity, and studies with APDs are in progress. Much more studies are needed to get some conclusion on this option.

12.3.5 Photon Detectors

The whole calorimeter system is designed to be located inside the superconducting solenoid of 3 Tesla. Thus photon detectors operational in strong magnetic field are needed. In the case of crystal calorimeter, the light yield is large and popular PIN silicon photodiode or APD can be used. On the other hand, in the case of sampling calorimeters, especially compensating calorimeters, the light yield is relatively poor and high-gain high-sensitivity photo-detector is needed.

One conventional solution is fine-mesh photomultiplier tubes (FMPMTs). This has been widely used for magnetic field below 1 Tesla. Possibility to improve its performace at higher magnetic field was first investigated.

Another option is hybrid devices such as Hybrid Photodiodes (HPDs) or Hybrid Avalance Photodiodes (HAPDs). Performances of such devices have been extensively studied so far. As the result, these hybrid devices are thought to be the best option at present.

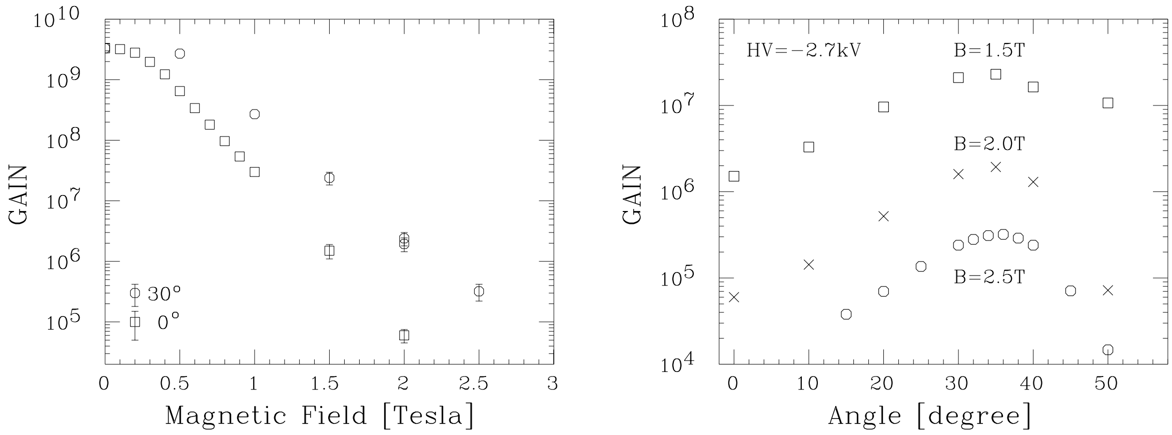

Figure 12.26: Magnetic field dependence of FMPMT gain. Horizontal axes are magentic field strength (left) and angle between magentic field and PMT axis (right).

1) FMPMT

In order to keep high gain even in the magnetic field of higher than 1 Tesla, high-gain FMPMTs with 24-stages of dynodes (Hamamatsu H2611SXA) were made and tested with magnetic field up to 2.5 Tesla using SKS spectrometer at KEK [13]. Fig. 12.26 shows magnetic field dependence of the gain. It still has gain of 3×10^5 at 2.5 Tesla when the angle bwtween the PMT axis and magnetic field was 30° even after rapid drop of gain with magnetic field. By extrapolation, it is expected to have gain of 3×10^4 at 3Tesla. However the gain variation with respect to field strength and PMT angle to the field direction is quite steep. This feature is not disireble, though is not fatal. We therefore concluded that FMPMT can not be the primary solution.

2) Hybrid Devices

HPD consists of a photo-cathode and a PIN photodiode facing to each other with a narrow vacuum gap in between. This is essentially insensitive to the axial magnetic field as is easily seen from the structure shown in Fig. 12.27. High-voltage is applied between the photocathode and the PIN silicon diode. Emitted photoelectrons are accelerated by this field, and injected to the PIN diode. Those photoelectrons deposits their energy when they pass the depletion layer and create electron-positron pairs. Roughly speaking,

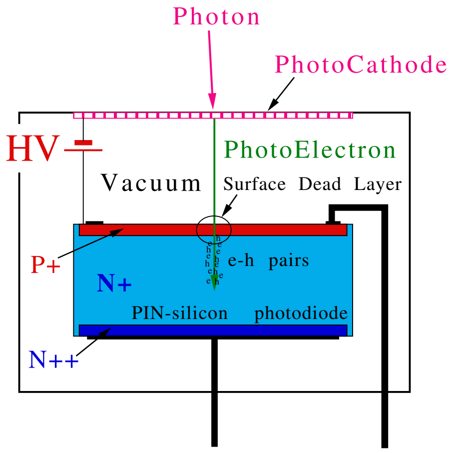

Figure 12.27: Schematic view of the HPD structure.

since excitation energy of one electron-position pair is 3.6 eV, gain of 3000 is expected with photo-cathode voltage of -11 kV. Actual gain is slightly lower due to the surface layer of the diode.

HAPD uses APD instead of PIN photodiode, and has higher gain due to the gain of APD itself. With an APD of gain 100, HAPD would achieve total gain comparable to PMTs.

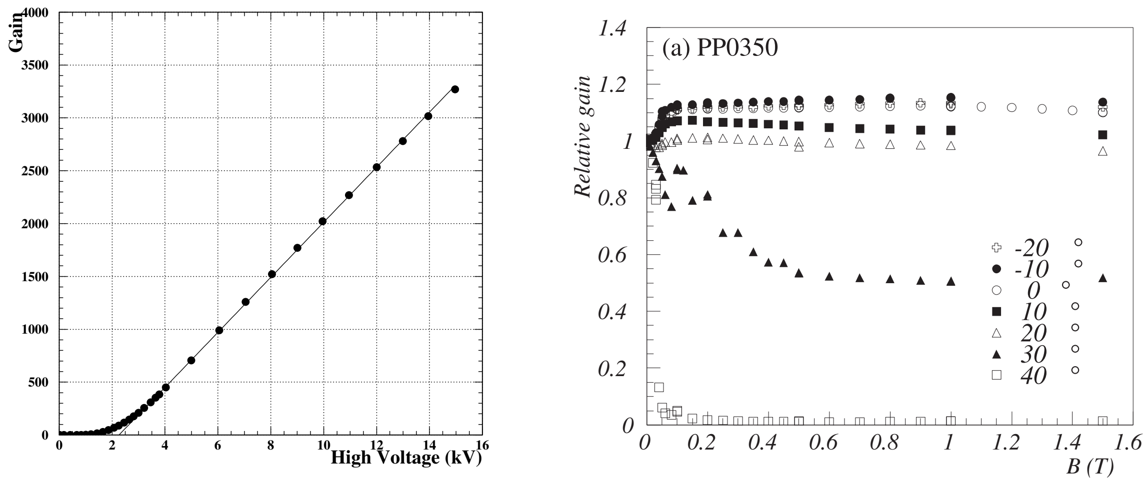

Figure 12.28: Gains of high-gain HPD out of (left) and in (right) a magnetic field.

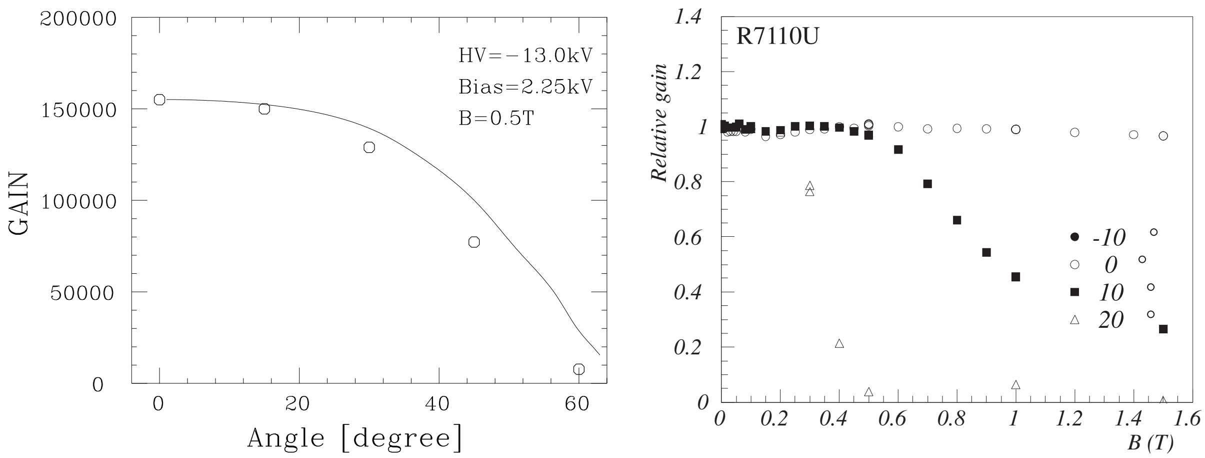

Figure 12.29: HAPD gain in a magnetic field for API 748-73-75-631 (left) and for Hamamatsu R7110U. Solid line in the left figure is result of calculation.

Properties of HPDs and HAPDs have been extensively studied so far [13, 14]. Gains of an HPD (Delft PP350F) in and out of magnetic field are shown in Fig. 12.28. The gain in the magnetic field with V_{PC}=15 kV was measured to be 4000. If we assume the photo-electron yield of EMC to be 260 p.e./GeV, preamp noise to be 1000 e^-, and HPD gain of 4000, we can achieve readout noise of about 1MeV.

Though the gain of HPDs is high enough for calorimetry, it is not high enough for PSD and SMD. We therefore studied performances of HAPDs. The gains of HAPDs were measured for 748-73-75-631 made by Advanced Photonix and for Hamamatsu R7110U in magnetic field, The results are shown in Fig. 12.29. It is clearly seen that HAPDs are operational in a magnetic field with high gain. It was aslo established that HAPDs had sensitivity to measure single photon as shown in Fig. 12.30. Therefore HAPDs can be a good candidate for PSD readout.

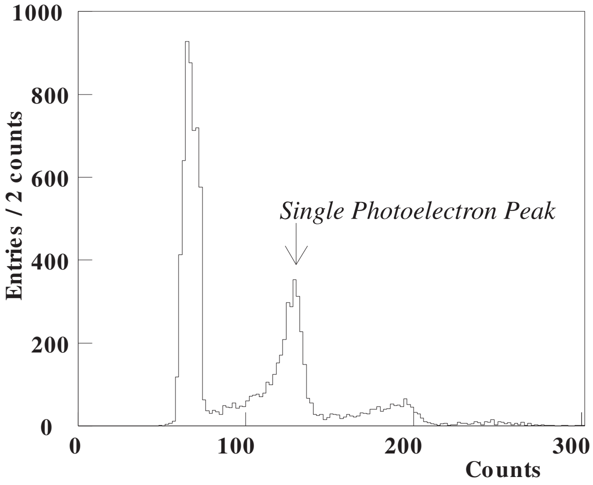

Figure 12.30: Single photo-electron peak measured outside of magnetic field by Hamamatsu R7110U.

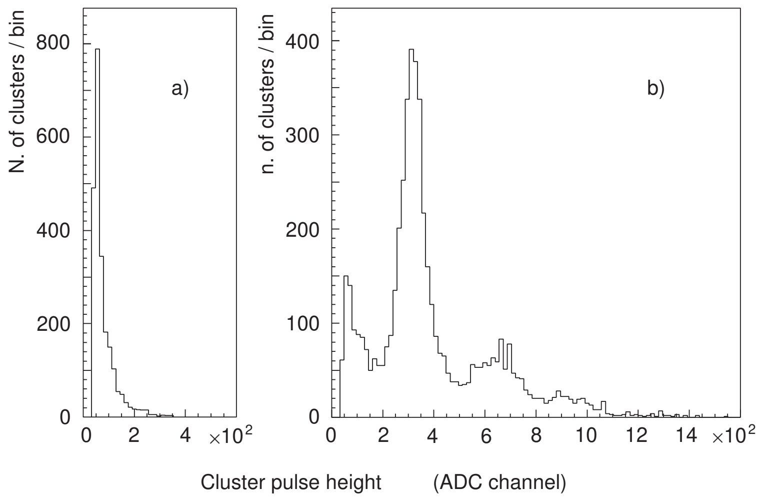

Figure 12.31: Single-photo-electron peak measured with electro-focus EBCCD by RD46.

Scintillator-strip SMD requires ultra-multi-channel photon detectors. Though once Advanced Photonix made 9-pixel HAPDs, it is not so easy to make multi-pixel HAPDs. Multi-channel HPDs are available with order of 100 channel/device at present. However sensitivity of HPDs are not high enough to use for SMD. Recently developed EBCCDs are ultra-multi-pixel devices naturally, and can achieve single-photon sensitivity [15, 16]. This is thought to be the best candidate for SMD, and basic surveys have been initiated. RD46 collaboration has succeeded to observe single photo-electron peak with an EBCCD as shown in Fig. 12.31. However it is an electro-focus type like image intensifiers, and can not be used in a magnetic field. We therefore started performance study on proximity-focused EBCCDs[15]. Structure of proximity-focused EBCCD is quite similar to that of HPDs shown in Fig. 12.27, replacing PIN silicon photodiode by an CCD. Photo-electrons bombard back-side of CCD, where substrait is thinned to enable photo-electrons to reach to the epitaxial layer. Fiber bundle with appropriate fiber spacing is attached to the photocathode window, and hits are reconstructed by clustering algorithm. Fig. 12.32 shows gain curve with respect to the applied photo-cathode voltage and noise vs. temperatire. Measured sensitivity is yet unable to detect single photon, and further studies are in progress.

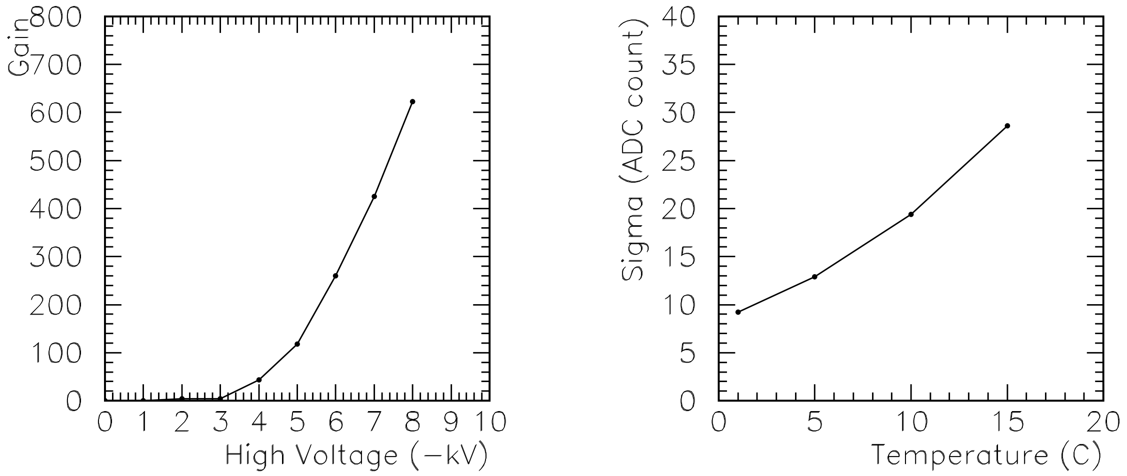

Figure 12.32: Gain vs. photo-cathode voltage (left) and noise vs. temperature (right) for proximity-focused EBCCD N7220.

12.3.6 Engineering R&Ds

There are several engineering issues related the actual construction of the calotrimeter system:

- Rigid and strong lead alloy;
- Mass production scheme and cost of tiles;
- Mass production scheme and cost of WLS assembly;
- Overall structure.

Most of these are yet open questions.

Our baseline design is to use lead alloy as absorber material. Test pieces made of Pb(Ca/Sn) alloy of several different concentrations have been made, and measurement of strength, Young's modulus, and creep are to be done soon. Feasibility of other options such as tungsten, copper, stainless steel or hybrid material such as CFRP-sandwiched lead are yet open question. However, copper or stainless steel would not be a solution if we stick to the baseline hadron energy resolution.

Machining of σ-grooves on tiles costs about \$10.00/tile for fabrication scale of a few thousand pieces. Since there are 2.2 million tiles in total, machining cost is significant. This can be solved by making tiles with casting. However, casting of tiles with σ-grooves seems very complicated, though is not impossible. On the other hand, the strip EMC option enables quite easy casting. Drastic cost reduction is expected by mega-strip casting ; casting of the strip array as a whole. This possibility should seriously be pursued.

Cost reduction of WLS assemly is totally an open question. Direct readout by attached photo-diode may eable us to avoid this problem.

There are two major ways to build the barrel calorimeter assembly. One is a stack of doughnuts, and the other is an assembly of orange sectors. Orange sector assembly is a natural solution for z-insertion of mega-tile. In this case, however, absorber plate orientation can not be perpendicular to the polar angle direction. Therefore sampling frequency, and accordingly energy resolution, becomes θ-dependent. One way to avoid this problem is to make a structure as shown in Fig. 12.33. This layout enables constant sampling frequency and at the same time reserving room for clear fibers, which increases as θ increases. However mechanical strength should be a very difficult problem.

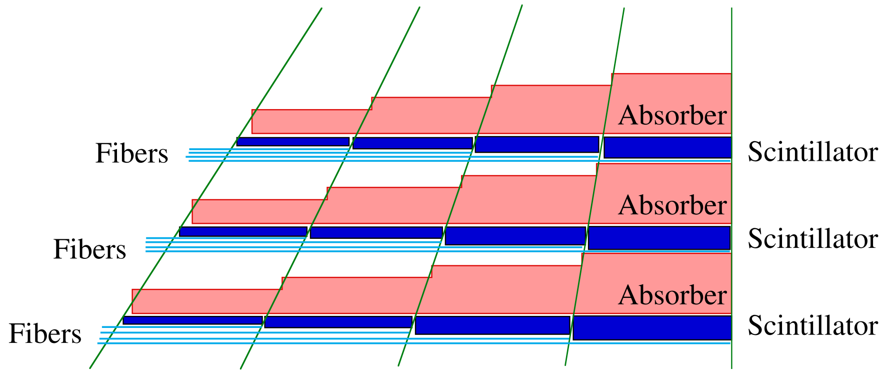

Figure 12.33: Conceptual layout of constant-sampling barrel calorimeter.

12.4 Simulation Study

A full simulator (named JIM) based on GEANT3 was constructed for detector parameter optimization and performance study. Calorimeter geometry and parameters listed in the Table 12.2 are implemented, together with all other detectors and structural components. Calorimeter signal normalization, response mapping, linearity and energy resolution examinations are inprogress, by comparing with the beam test results.

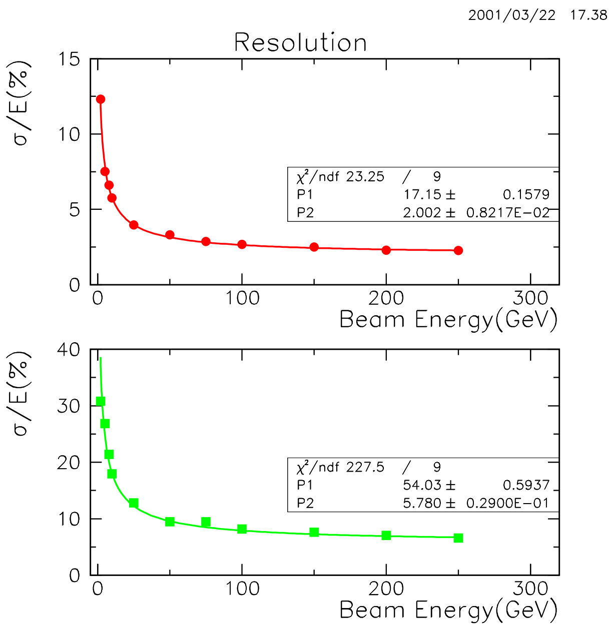

Figure 12.34: Energy resolution of barrel calorimeter implemented in a full simulator. Top is for electrons, and bottom is for pions

Fig. 12.34 shows full simulation result of the energy resolution of barrel calorimeter for electrons and for pions. Obtained hadron energy resolution of $54\%/\sqrt{E}\oplus 5.8\%$ is much worse than our beam test results shown in Fig. 12.17, and more tuning of detailed geometry and/or cross section of physics processes are necessary.

Response mapping was also done using electrons with respect to the azimuthal angle as shown in Fig. 12.35. We observe a dip in energy measurement at the super-tower boundary. The beamtest data, however, shows enhancement rather than dip as shown in Fig. 12.20. This difference is considered to be caused by two reasons: 1)tile non-uniformity is not implemented into the full simulator, and 2)there exists unexpected gap between supertowers in the geometry definition. The latter was found by difference of response map between electron injection and positron injection, and should be fixed. Impact of non-uniformity on physics analysis should be investigated to know necessity to implement non-uniformity into the full simulator.

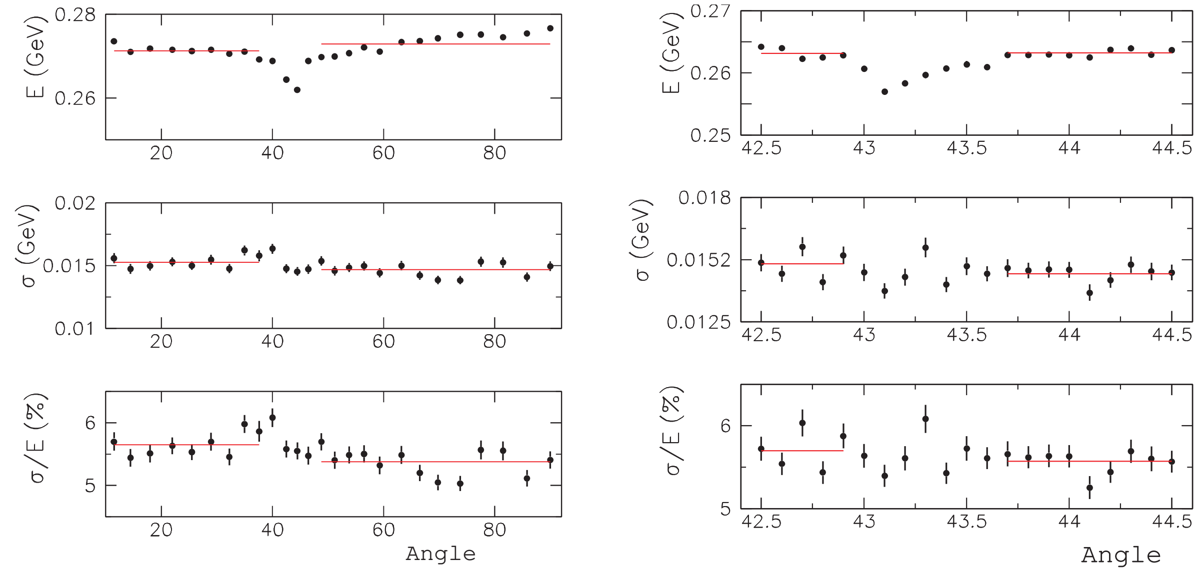

Figure 12.35: Calorimeter response vs azimuthal angle obtained by 10 GeV electron injection. Dips in the left and right figures show boundary between the endcap and barrel calorimeters and boundary between barrel super-towers, respectively.

12.5 Future Prospect

Results of quick simulation for various physics processes have demonstrated that the baseline calorimeter system can realize excellent physics sensitivity. However, validation with a full simulation is essentially important, especially for optimization of granularity. This must be completed urgently.

Extensive hardware studies have proven the technical feasibility and performance of tile/fiber scheme with hardware compensation. There are still open questions in high-granularity EMC option and in photon detector options. These issues are also related to the total cost, and thus should be solved before moving to the proto-type R&D stage. Engineering studies including the heavy metal choice should also be finished before the proto-type stage.

Those studies must be completed in JFY 2001 and 2002.

Bibliography

[1] H.P.Wellisch, J.P.Kubenka, H.Oberlack and P.Schacht, MPI-PhE/94-03

[2] E.Bernardi et.al., Nucl.Instr.Meth.A262(1987)229

[3] K.Ishii et.al., Nucl.Instr.Meth.A385(1997)215

[4] R.Wigmans, Nucl.Instr.Meth.A259(1987)389

[5] D.Acosta et.al., Nucl.Instr.Meth.A308(1991)481

[6] T.Suzuki et.al., Nucl.Instr.Meth.A432(1999)48

[7] G.Drew et.al., Nucl.Instr.Meth.A290(1990)335

[8] H.Miyata, Ph.D. thesis, University of Tsukuba (1984)

[9] S.Uozumi et.al., Submitted toNucl.Instr.Meth.

[10] F.Kajino et.al., Nucl.Instr.Meth.A383(1996)260

[11] K.Kawagoe et.al., Submitted toNucl.Instr.Meth.

[12] D.Acosta et.al., Nucl.Instr.Meth.A302(1991)36-46

[13] Y.Fujii et.al., Nucl.Instr.Meth.A366(1995)71

[14] N.Kanaya et.al., Nucl.Instr.Meth.A421(1999)512

[15] S.Suyama et.al., SPIE Vol.3173(1997)422
EB-CCD N7220 Data Sheet, Hamamatsu Photonix Inc.

[16] S.Buontempo et.al., Nucl.Instr.Meth.A413(1998)255